

# Add-Drop Filter and Refractive Index and Temperature Sensor Using 2D Photonic Crystal Ring Resonator

Puja Sharma<sup>a</sup>, Nilaksha Ghosh<sup>a</sup>, Man Mohan Gupta<sup>b</sup>, and Sarang Medhekar<sup>a,\*</sup>

<sup>a</sup>Department of Physics, Central University of Jharkhand, Ranchi, India

<sup>b</sup>Department of Physics, Tata College Chaibasa, West Singh Bhum, India

\*Corresponding author email: [sarang.medhekar@cuja.ac.in](mailto:sarang.medhekar@cuja.ac.in), [smedhekarbit@gmail.com](mailto:smedhekarbit@gmail.com)

Regular paper: Received: Mar. 05, 2023, Revised: June. 11, 2023, Accepted: June. 13, 2023,  
Available Online: June. 15, 2023, DOI: 10.52547/ijop.16.2.221

**Abstract**— In this paper, a structure is proposed using ring resonator created on 2D photonic crystal (PC) that acts as an add-drop filter (ADF) in all-optical communication systems. The same structure can also act as refractive index (RI) and temperature sensor. The structure is made up of a hexagonal lattice of air holes in a dielectric slab of silicon with the refractive index of 3.46. The band diagram of the considered structure is obtained using plane wave expansion (PWE) method, and optical propagation through it is simulated using finite difference time domain (FDTD) method. The computational analysis is performed on different structural and physical parameters. Transmission efficiency, quality factor and bandwidth are investigated by varying (i) lattice constant (ii) radius of holes of different parts of the structure and (iii) refractive index of different parts of the structure. The chosen parameters result in operating wavelength around 1550 nm. The designed ADF has a footprint of only  $68\mu\text{m}^2$  and a dropping efficiency of 100%. The sensitivity of the structure is determined by determining shifts in the resonance wavelength as a function of the RI of the holes/slab. The designed structure exhibits desirable features like (i) narrow bandwidth of 1.5 nm, (ii) high-quality factor of 1033, (iii) low detection limit of  $3.6 \times 10^{-4}$  RIU, (iv) high RI sensitivity of 407 nm/RIU, and (v) high temperature sensitivity of 104 pm/K.

**KEYWORDS:** Photonic Crystal, Finite Difference Time Domain Method, Plane Wave Expansion Method, Add-Drop Filter.

## I. INTRODUCTION

Photonic crystals (PCs) are artificial structures with periodic variations of refractive index in different directions. Light propagation through PCs is restricted in certain directions for a given frequency range, giving rise to a photonic band gap (PBG). The creation of point and line defects in PCs allows for the localization of light in the defect area [1]. By employing point defects, light is captured in specific locations. It's a type of optical microcavity/ ring resonator in which the modal volume can be very small but have a very high-quality factor [2]. PCs are suitable for all-optical devices and components due to their ultra-compact size, faster speed, flexible design capability, and low interaction [3]. Wavelength division multiplexing (WDM) systems rely heavily on add-drop filters (ADFs). ADF is a common element in switching and filtering operations too. Silicon-based ADFs have the potential to be used in refractive index (RI) sensing. Integrated silicon photonic RI sensors are widely used in medical diagnostics, environmental monitoring, industrial applications, food safety, and chemical analysis [4]. PC sensors are sensitive to external disturbances such as changes in pressure and temperature [5]. These sensors have received a lot of attention in recent years because of their high sensitivity, high-quality factor, small volume, and low detection limit [6]. In recent years, photonic-integrated RI sensors have been extensively researched and evaluated. These on-chip silicon photonic devices offer a potentially promising sensing device due to their low cost, compact size,

large-scale integration, good stability, and high energy efficiency [7]. Several RI based sensors are present in the literature like pressure sensor[8], chemical sensor [9], temperature sensors [6], humidity sensor [10], and biosensor [11], etc. based on various device structures such as cavities [12], Mach-Zehnder interferometers (MZI) [13] and ring resonators[3], etc.

Generally, ADFs are composed of two waveguides, the BUS and DROP waveguides, which are linked by a circulating resonant cavity. When a multi-wavelength signal travels through the BUS waveguide, the resonant cavity is excited for a specific wavelength (resonance wavelength), which is transferred at the forward or backward DROP port of the drop waveguide. ADFs that eliminate cross-talk between the BUS and the DROP over a wide frequency range are always preferred [14]. By properly engineering the BUS/ring coupling scheme within the ADF, forward and backward dropping at resonant wavelengths can be achieved. Due to high-quality factors and low loss in ultra-compact cavities, ring resonator-based ADFs are mostly preferred [15].

The hexagonal ring resonator of the proposed ADF and RIT sensor is the same as that presented in the paper [16], [17]. To comprehend dropping efficiency, bandwidth, and quality factor, performance of ADF has been investigated for different parameters such as (i) lattice constant, (ii) radius of the holes in different parts of the design, and (iii) refractive index of different parts of the design. The structural parameters are chosen to have operating wavelength of the device around 1550 nm.

The proposed structure can also sense RI and T simultaneously. Its sensing performance is determined by studying the effect of variation of the refractive index of holes ( $n_0$ ) and slab ( $n$ ) on the resonance wavelength. RI sensitivity is calculated by varying the RI of the background air hole from 1.01 to 1.05 in the steps of 0.01 and then Temperature sensitivity is determined in the range of 305K – 325K. The designed sensor exhibits desirable features

like (i) narrow bandwidth of 1.5 nm (ii) high-quality factor of 1.033 (iii) low detection limit of  $3.6 \times 10^{-4}$  RIU at a resonance wavelength of 1550 nm (iv) high RI sensitivity of 407 nm/RIU and (v) high Temperature sensitivity of 104 pm/K.

Design of the proposed sensor follows below mentioned points.

1. The lattice constant is adjusted to have the operating wavelength of the sensor in the telecommunication range (good sources and detectors are easily available at telecommunication wavelengths).
2. The ring resonator should have a resonant wavelength in the telecommunication range.
3. The refractive index of the slab should be realistic.
4. The structure parameters are chosen to have the ring resonator of the sensor exhibiting high quality factor, high sensitivity and low detection limits.
5. The sensor structure should be as simple as possible (should be homogeneous in terms of the holes' positions and radius) to minimize difficulty in fabrication.

The remaining of the paper is organized as follows; in the Section II, we present the design and bandgap analysis of the ADF. Numerical investigations and results are discussed in Section III. Performance analysis for variation of different structural parameters is presented in Section IV. The sensing performance is presented in Section V. Finally, Section VI concludes the paper.

## II. THE PROPOSED STRUCTURE AND BAND GAP ANALYSIS

The proposed ADF is based on 2D hexagonal lattice PCs comprising of  $29 \times 21$  air holes (X-Z plane) in Silicon slab of refractive index 3.46 [11] as shown in Fig. 1. The radius ( $r$ ) of air holes is  $0.295a$ , where  $a$  is the lattice constant and is chosen to be 333 nm. It has two defect waveguides. The upper (BUS) waveguide is

coupled to the lower (DROP) waveguide through a hexagonal-shaped cavity. The cavity is consisting of coupling holes (blue color), inner holes (red color), adjacent holes (green color), and corner holes (cyan color) having radii  $r_1$ ,  $r_2$ ,  $r_3$ , and  $r_4$  respectively.  $r_1 = r_2 = r_3 = r_4 = r$  has been considered to initiate numerical investigations. Ports A, B, C, and D are used as input ports, transmission ports, forward-dropping ports, and backward-dropping ports respectively.

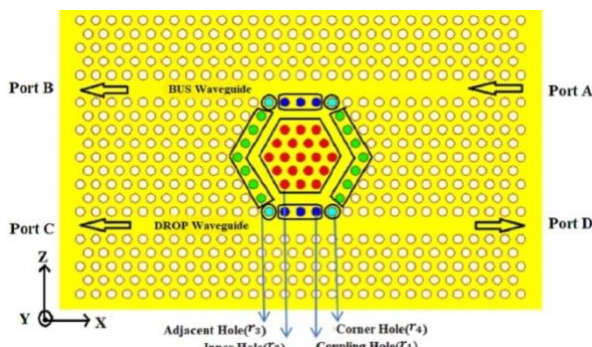


Fig. 1. Schematic design of optical add-drop filter.

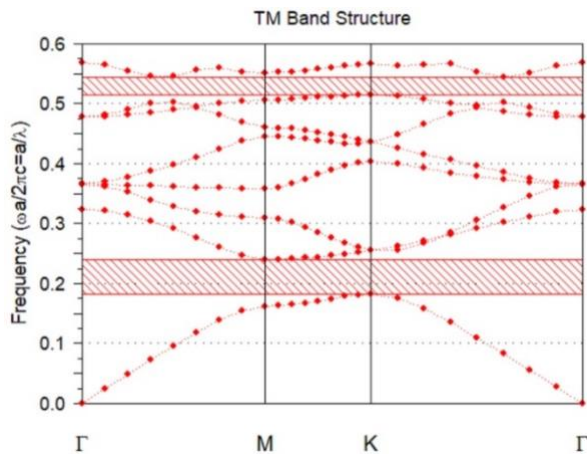


Fig. 2. Band structure of the proposed structure for TM polarization.

The band diagram of the considered structure for the above-mentioned parameters is shown in Fig. 2 which has been obtained using the PWE method [18]. As can be seen, the structure offers two PBG of normalized wavelength in the range  $0.183 < a/\lambda < 0.243$  and  $0.518 < a/\lambda < 0.549$  which correspond to free space wavelengths in the range  $1218\text{nm} < \lambda < 1617\text{nm}$  and  $539\text{nm} < \lambda < 571\text{nm}$  respectively for TM polarization (Magnetic field is perpendicular to plane X-Z).

### III. NUMERICAL INVESTIGATION AND RESULTS

A Gaussian optical temporal light pulse centered at wavelength of 1550 nm is launched at input port A of Fig. 1 and normalized transmission spectrum is obtained by performing a Fast Fourier Transform of the time responses at the transmission port B, forward drop port C, and backward drop port D as shown in Fig. 3.

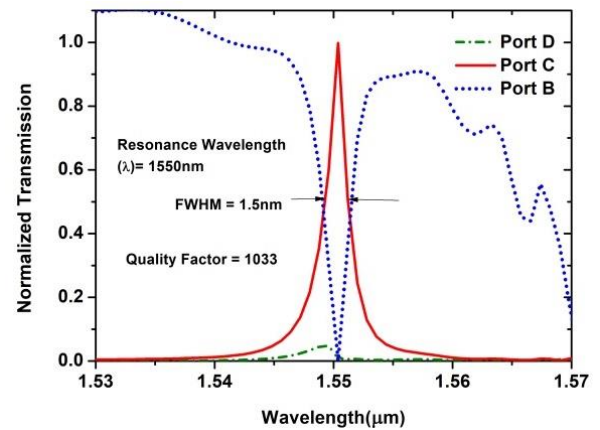


Fig. 3. Normalized transmission at different ports of proposed ADF.

As evident in the figure, at the wavelength 1550 nm, the hexagonal ring offers maximum coupling between upper and lower defect waveguides, and hence, the optical power injected into port A mostly appears at forward dropping port C. The wavelength 1550 nm is therefore the resonant wavelength of the proposed ADF. For an off-resonant wavelength (e.g. at 1544nm) the coupling between the two waveguides is feeble and optical power injected into port A mostly appears at transmission port B. To obtain steady-state magnetic field patterns in “On resonance” and “Off-resonance” conditions, we launch continuous wave (CW) of wavelengths 1550 nm and 1544 nm separately at input port A. The steady-state magnetic field for the mentioned cases has been shown in Fig. 4 (a) and 4 (b) respectively. It is very clear from these figures that for resonance wavelength of 1550nm, injected light couples through the resonant cavity and appears at the forward dropping port C and for off-resonance of 1544nm it appears at transmission port B only.



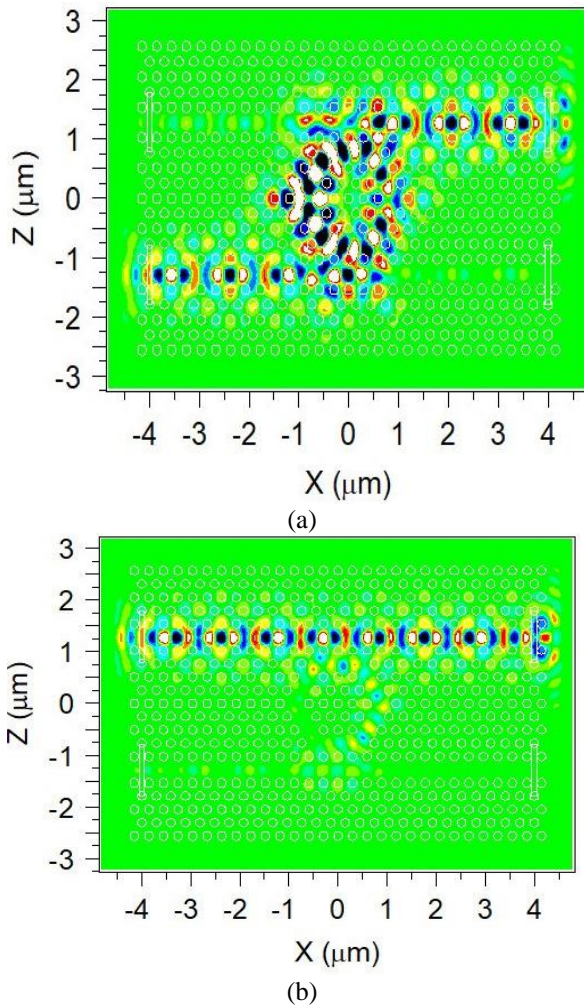


Fig. 4. Steady-state magnetic field distribution for (a) on resonance wavelength 1550 nm and (b) off-resonance wavelength 1544 nm.

It is seen that the forward drop efficiency (normalized transmission at port C) at the resonant wavelength is 100%. The efficiency of ADF is measured by the Quality factor  $Q = \lambda / \text{FWHM}$  where  $\lambda$  is resonance wavelength and full-width at half maximum (FWHM) is spectral line width (FWHM) [19]. The calculated values of the quality factor and spectral line width of the proposed ADF are 1033 and 1.5 nm respectively and are suitable for WDM systems.

#### IV. PERFORMANCE OF THE ADF

Now, we study the performance of ADF in detail, for variation of different structural parameters like lattice constant, the radius of different holes, and Physical parameters like the refractive index of different parts.

##### A. Performance with different lattice constants

To analyse the effect of the lattice constant on the performance of the ADF, we vary the lattice constant ( $a$ ) from 332nm to 334nm in the step of 1 nm, keeping all other parameters of Fig. 1 unchanged. The normalized transmission spectrum obtained at forwarding dropping port C of ADF is shown in Fig. 5. Further, the performance of ADF with the variation of lattice constant is tabulated in Table 1.

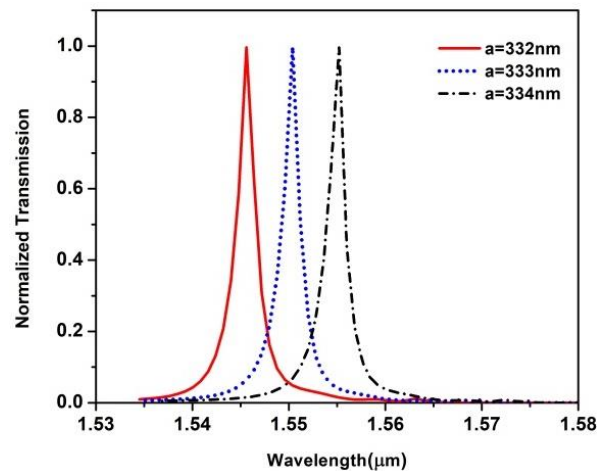


Fig. 5. Normalized transmission spectrum at forward dropping port C for varying lattice constant,  $a$

Table 1. Performance of ADF for different lattice constants  $a$ .

$a$ (nm)	FWHM (nm)	$\lambda$ (nm)	Q	T (%)
332	1.5	1545.59	1030.39	99.6
333	1.5	1550.39	1033.59	99.7
334	1.5	1555.20	1036.80	99.7

It is clear from Table 1 that on an increase in the value of lattice constant, resonant wavelength and quality factor increase while spectral width remains unchanged.

##### B. Performance with different radius of holes

The dimensions of air-filled cylindrical holes in slabs also affect the performance of the ADF. Hence, we analyse the performance of the designed ADF for different radii of holes of different parts of the ADF. Keeping all other parameters of Fig. 1 unchanged, the radius of all holes ( $r$ ), coupling holes ( $r_1$ ), inner holes ( $r_2$ ), adjacent holes ( $r_3$ ), and corner holes ( $r_4$ ) are varied one-by-one from  $0.29a$  to  $0.3a$  and corresponding normalized

transmission spectra at forward dropping port C are obtained.

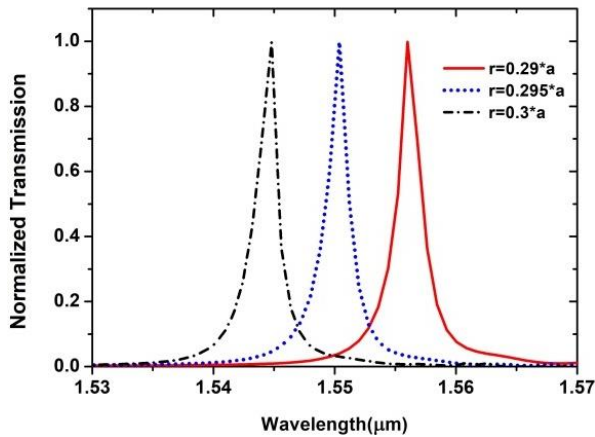


Fig. 6. Normalized transmission spectrum at forward dropping port C for varying radius,  $r$ , of all holes.

### C. Performance with different radius of all holes

A change in the radius of all holes in the slab will lead to a change in the PBG which will affect the performance of the ADF. An increase in radius  $r$  of all holes (shown with white color in Fig. 1) of the structure results in a shift of resonance peak towards the lower wavelength side (blue shift) as shown in Fig. 6. It can be noticed from the figure that the designed ADF is having 100% dropping efficiency. The performance of the ADF for different  $r$  is given in Table 2.

Table 2. Performance of ADF for variation of radius ( $r$ ) of all holes of the structure

$r$ (nm)	FWHM (nm)	$\lambda$ (nm)	Q	T (%)
0.29a	1.5	1556.01	1037.34	99.7
0.295a	1.5	1550.39	1033.59	99.7
0.3a	1.5	1544.79	1029.86	99.7

From Table 2 it is clear that resonance wavelength and Quality factor (Q) decrease with an increase in radius,  $r$ . Radius  $r$  does not affect the spectral line width of ADF.

### D. Performance with different radius of coupling holes

Coupling holes (shown in blue color in Fig. 1) couple the light propagating in the BUS waveguide to the DROP waveguide through a hexagonal shape cavity. As shown in Fig. 7, the resonance peak shifts towards the lower

wavelength side (blue shift) with the increase of radius ( $r_1$ ) of coupling holes. The performance of the ADF for varying radius ( $r_1$ ) is tabulated in Table 3.

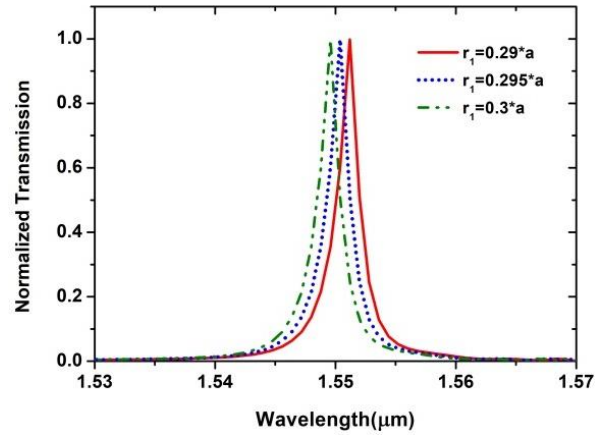


Fig. 7. Normalized transmission spectrum at forward dropping port C for varying radius ( $r_1$ ) of coupling holes.

Table 3. Performance of ADF for variation of radius ( $r_1$ ) of coupling holes of the structure.

$r_1$ (nm)	FWHM (nm)	$\lambda$ (nm)	Q	T (%)
0.29a	1.5	1551.18	1034.12	99.8
0.295a	1.5	1550.39	1033.59	99.7
0.3a	1.5	1549.59	1033.06	99.6

Simulations show that coupling holes with radius  $r_1 = 0.29a$ ,  $0.295a$  and  $0.3a$  produce forward dropping efficiency of 100%.

### E. Performance with different radius of inner holes

The normalized transmission spectrum for varying radii ( $r_2$ ), of inner holes (shown in red color in Fig. 1) is shown in Fig. 8. It reveals that the resonant peak shifts to a lower value of wavelength with an increasing radius of inner holes ( $r_2$ ). The performance of the ADF for varying radii ( $r_2$ ) is tabulated in Table 4.

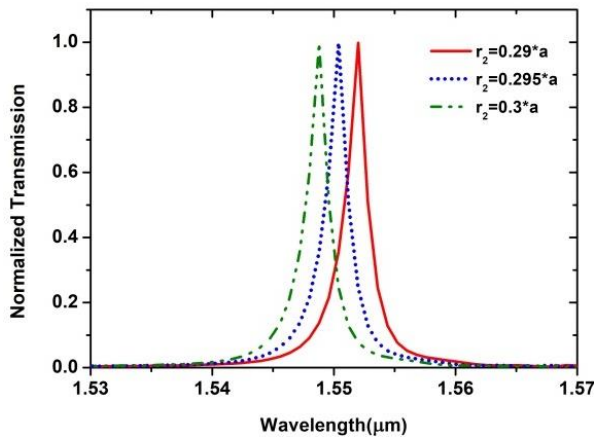


Fig. 8. Normalized transmission spectrum at forward dropping port C for varying radius ( $r_2$ ) of inner holes.

Table 4. Performance of ADF for variation of radius ( $r_2$ ) of inner holes of the structure.

$r_2$ (nm)	FWHM (nm)	$\lambda$ (nm)	Q	T (%)
$0.29a$	1.5	1551.99	1034.66	99.6
$0.295a$	1.5	1550.39	1033.59	99.7
$0.3a$	1.5	1548.79	1033.52	99.8

Quality factor  $Q$  decreases on increasing the radius of inner holes ( $r_2$ ). Spectral linewidth remains constant with an increasing value of ( $r_2$ ).

#### F. Performance with different radius of adjacent holes

Variation of normalized transmission spectrum with the varying radius of adjacent holes (shown with green color in Fig. 1) is shown in Fig. 9 which shows that resonance peak shifts towards lower wavelength side with an increase of radius ( $r_3$ ) of adjacent holes. The performance of the ADF for varying radii ( $r_3$ ) is tabulated in Table 5.

Table 5. Performance of ADF for variation of radius ( $r_3$ ) of adjacent holes of the structure.

$r_3$ (nm)	FWHM (nm)	$\lambda$ (nm)	Q	T (%)
$0.29a$	1.5	1551.99	1034.66	99.7
$0.295a$	1.5	1550.39	1033.59	99.7
$0.3a$	1.5	1549.79	1033.52	99.7

Tabulated data show that the Quality factor decreases on increasing the radius ( $r_3$ ) of adjacent holes. Spectral line width remains constant with increasing values of ( $r_3$ ).

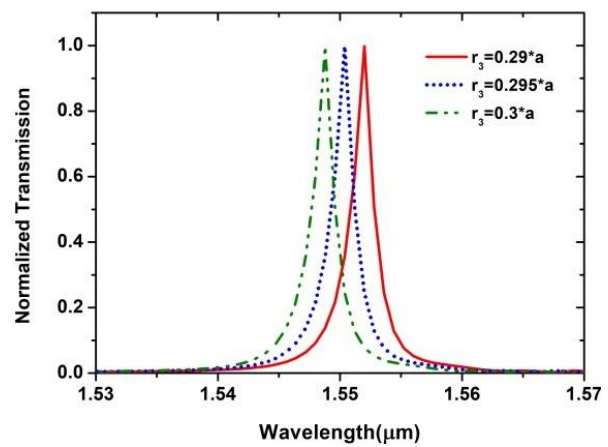


Fig. 9. Normalized transmission spectrum at forward dropping port C for varying radius ( $r_3$ ) of adjacent holes.

#### G. Performance with different radius of corner holes

The normalized transmission spectrum for varying radii ( $r_4$ ) of corner holes (shown with cyan color in Fig. 1) is shown in Fig. 10. Resonant peak shifts to a lower value of wavelength with an increasing radius of corner holes ( $r_4$ ). The performance of the ADF for varying radii ( $r_4$ ) is given in Table 6.

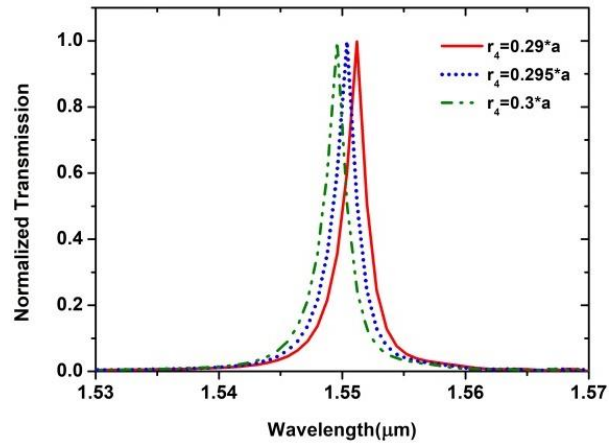


Fig. 10. Normalized transmission spectrum at forward dropping port C for varying radius ( $r_4$ ) of corner holes.

Table 6. Performance of ADF for variation of radius ( $r_4$ ) of adjacent holes of the structure.

$r_4$ (nm)	FWHM (nm)	$\lambda$ (nm)	Q	T (%)
$0.29a$	1.5	1551.19	1034.12	99.6
$0.295a$	1.5	1550.39	1033.59	99.7
$0.3a$	1.5	1549.59	1033.06	99.7

Quality factor,  $Q$ , decreases on increasing the radius of corner holes ( $r_4$ ). Spectral linewidth remains constant with an increasing value of  $r_4$ .



H. Effect of change of refractive index

ADF provides the tuning to the desired wavelength based on a slight variation of the refractive index. Hence, in this part, we investigate the performance of the proposed ADF for variation of refractive index ( $n$ ) of slab and background index of all holes ( $n_0$ ), coupling holes ( $n_1$ ), inner holes ( $n_2$ ), adjacent holes ( $n_3$ ), and corner holes ( $n_4$ ). Keeping all other parameters of Fig. 1, we vary the refractive index of the slab from 3.45 to 3.47 and the background index of different holes from 1.01 to 1.05 with an increment of 0.01. The effect on behavior (transmission at forward dropping port C) and performance of the proposed ADF for the individual case are discussed below.

I. Effect of change of refractive index ( $n$ ) of the slab

Normalized transmission spectrum at forwarding dropping port C is obtained for increasing the value of the refractive index of the slab,  $n$ , and is shown in Fig. 11. Results show that increasing the value of the refractive index of the slab shifts the resonant peak to a higher wavelength side (red shift).

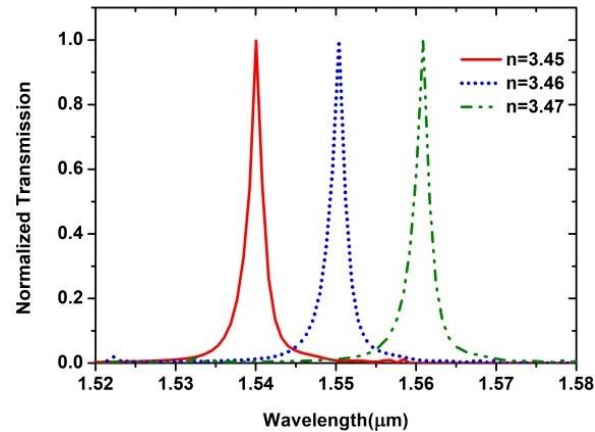


Fig. 11. Normalized transmission spectrum at forward dropping port C for varying refractive index,  $n$  of the slab.

The performance of ADF for the different refractive indexes of the slab is tabulated in Table 7 which shows Quality factor  $Q$  increases and spectral line width remains constant with an increase in the refractive index of the slab.

Table 7. Performance of ADF for variation of refractive index ( $n$ ) of slab.

$n$	FWHM (nm)	$\lambda$ (nm)	$Q$	T (%)
3.45	1.5	1540.04	1026.69	99.6
3.46	1.5	1550.39	1033.59	99.7
3.47	1.5	1560.87	1040.58	99.7

3.45	1.5	1540.04	1026.69	99.6
3.46	1.5	1550.39	1033.59	99.7
3.47	1.5	1560.87	1040.58	99.7

J. Effect of change of background index ( $n_0$ ) of all holes

Variation of transmission at port C for different values of background index ( $n_0$ ) of all holes is shown in Fig. 12 and the performance of ADF for the same is tabulated in Table 8.

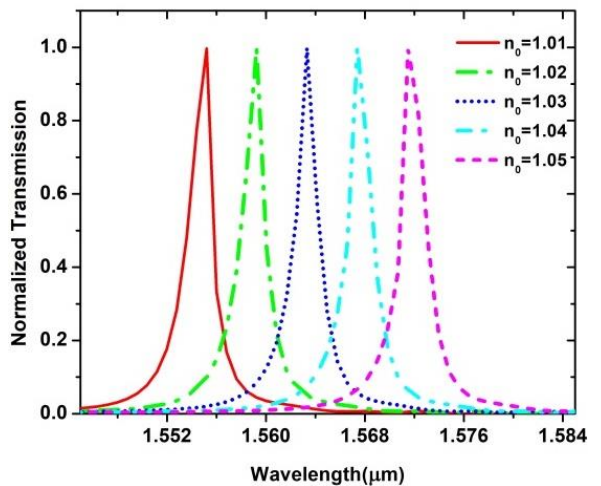


Fig. 12. Normalized transmission spectrum at forward dropping port C for varying background index ( $n_0$ ) of all holes.

Table 8. Performance of ADF for variation of background index ( $n_0$ ) of all holes

( $n_0$ )	FWHM (nm)	$\lambda$ (nm)	$Q$	T (%)
1.01	1.5	1555.21	1036.80	99.7
1.02	1.5	1559.25	1039.50	99.7
1.03	1.5	1563.31	1042.21	99.7
1.04	1.5	1567.40	1044.93	99.7
1.05	1.5	1571.50	1047.66	99.7

It is evident from simulations that increasing the background index ( $n_0$ ) of all holes of ADF tunes the resonant wavelength to a higher value with 100% dropping efficiency and constant spectral line width whereas the Quality Factor  $Q$  increases with an increase in the background index of all holes.

K. Effect of change of background index of different holes

Now, the background index of coupling holes ( $n_1$ ), inner holes ( $n_2$ ), adjacent holes ( $n_3$ ), and corner holes ( $n_4$ ) is varied individually, and the

effect on transmission at forward dropping port C for each case is studied.

Simulation shows that variation of the background index of different holes produces almost a negligible or zero shift in resonant wavelength. Spectral linewidth remains the same for variation in the background index (from 1.01 to 1.05) of coupling holes, inner holes, adjacent holes, and corner holes.

It is worth mentioning here that the Quality Factor of the proposed structure may further be increased by employing scattering rods, shifting the resonant cavity holes position, or incorporating more than one layer of holes between cavity design and BUS/DROP waveguides [20].

## V. THE SENSOR

Based on the above investigations and to have a device operating wavelength around 1550 nm the structure parameters are fixed as  $a=333\text{nm}$ ,  $r = 0.295a$ ,  $n = 3.46$  (Si), and  $n_0 = 1$ . Table 9. Shows the basic formula used for the proposed sensor [11].

Table 9. Shows the basic formula used for the proposed sensor.

Calculated parameter	Formula	unit
Normalized Transmission	$T = P_{\text{out}}/P_{\text{in}}$	
Quality factor (Q)	$Q = \lambda/\text{FWHM}$	
RI Sensitivity (S)	$\Delta\lambda/\Delta n$	Nm/RIU
Temperature Sensitivity ( $S_T$ )	$\Delta\lambda/\Delta T$	Pm/K
detection limit (DL)	$\lambda/(10QS)$	RIU

Where  $P_{\text{out}}$  and  $P_{\text{in}}$  are output power and input power respectively.  $\lambda$  is the resonance wavelength, FWHM, is the full width at half maximum,  $\Delta\lambda$  is the shift in resonance wavelength,  $\Delta n$  is the change in RI and  $\Delta T$  is the change in Temperature.

Having structure parameters finalized the performance of the proposed structure in terms of the RI sensor and temperature sensor is discussed in the following sections.

### A. RI Sensitivity

To evaluate the RI sensitivity of the proposed structure, the temperature is considered constant at  $T=300\text{ K}$  and the RI of air holes is varied in the range of 1.01 to 1.05 with an increment of 0.01 and a shift in the resonant wavelength is noted which is as shown in Fig. 12. Accordingly, the RI sensitivity is calculated as 407 nm/RIU.

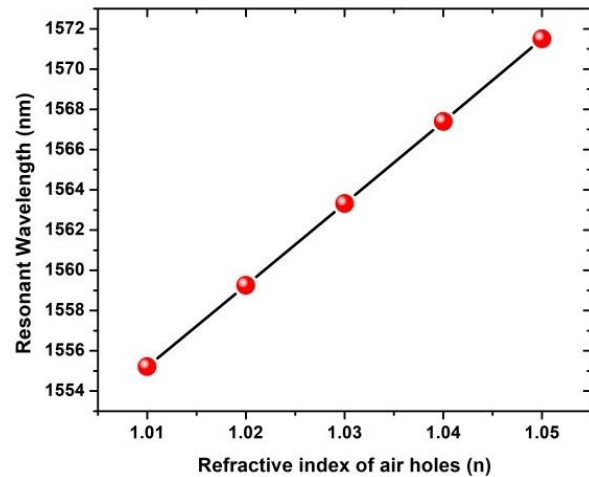


Fig. 13. Shifts of resonant wavelength by varying the RI of air holes.

Table 10. Performance of the proposed RI sensor

Refractive index (RI)	Resonant wavelength (nm)	The shift in resonant wavelength (nm)
1.01	1555.21	-
1.02	1559.25	4.04
1.03	1563.31	4.06
1.04	1567.40	4.09
1.05	1571.50	4.10

Table 10 shows the performance of the proposed RI sensor. It may be noted here that relationship between RI and resonant wavelength shift is almost linear as shown in Fig. 13.

The effect of resonant wavelength shift for a wide range of RI change (from 1 to 2) is shown in Fig. 14 and Table 11 shows the corresponding performance.



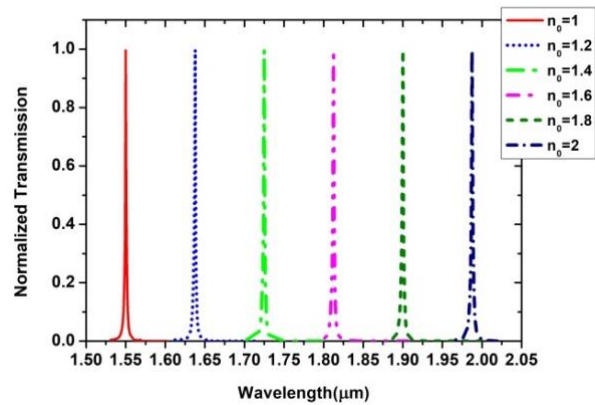


Fig. 14 Normalized transmission spectrum at forward dropping port C for varying background index ( $n_0$ ) of all holes for RI change from 1 to 2.

Table 11. Performance of the proposed RI sensor for RI change (from 1 to 2)

Refractive index (RI)	Resonant wavelength (nm)	The shift in resonant wavelength (nm)
1	1550.39	-
1.2	1637.80	87.41
1.4	1724.98	87.18
1.6	1812.53	87.55
1.8	1900.12	87.59
2	1987.51	87.39

B. Temperature Sensitivity

The temperature sensing mechanism exploits a larger thermo-optic coefficient of the silicon slab ( $10^{-4}$ ) [22]. Refractive index of the Si slab changes as the temperature rises resulting in a shift in the resonant wavelength. The thermo-optic coefficient of air ( $10^{-7}$ ) is much smaller and therefore its RI may be considered equal to unity ignoring any change in it [23]. The RI of the Si slab ( $n_1$ ) can be expressed as  $n_1 = n_0 + \alpha \Delta T$ , where  $n_0$  is the RI at a given temperature and  $\alpha$  is the thermo-optic coefficient ( $2.4 \times 10^{-4}$ ) of the silicon slab and  $\Delta T$  is the temperature change.

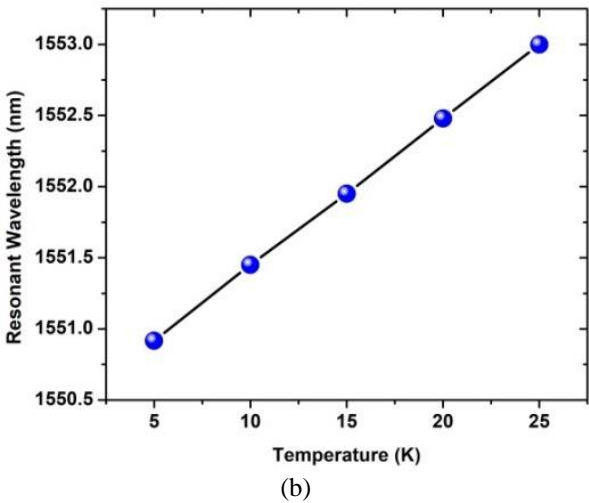
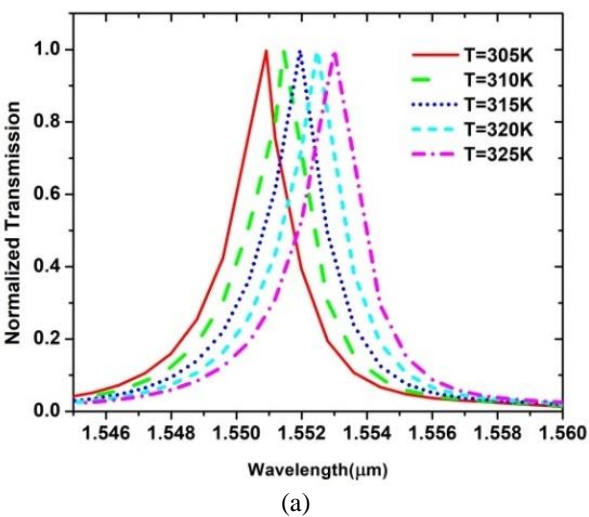


Fig. 15. (a) Normalized transmission spectrum for varying the Temperature of Si slab (b) Shifts of resonant wavelength by varying the Temperature of Si slab.

Table 12. Performance of the proposed Temperature sensor.

RI change due to thermo-optic effect (n)	Corresponding temperature (K)	Resonant wavelength (nm)	Resonant wavelength shift (nm)
3.4612	305	1550.92	-
3.4624	310	1551.44	0.52
3.4636	315	1551.95	0.51
3.4648	320	1552.47	0.52
3.4660	325	1552.99	0.52

The normalized transmission spectrum of the proposed structure at various temperatures of the silicon slab is shown in Fig. 15(a). We revealed that a change in the temperature of the Si slab by 5K results in a 0.0012 change in its RI. As T increases, the resonant wavelength shifts toward the higher wavelength (red-

shifted) side in the output spectrum. Furthermore, as shown in Fig. 15(b), the redshift is almost linear with T. Table 12 shows the effectiveness of the proposed temperature sensor. The calculated temperature sensitivity is 104 pm/K. The suggested sensor can measure both temperature and refractive index simultaneously. Table 13 also compares the proposed sensor with previously published sensors.

Table 13. Comparison of the proposed sensor with previously published designs.

References	Type of device	Temperature sensitivity (pm/K) or (pm/ $^{\circ}$ C)
[17]	Cascaded cavities up and down	76
[24]	super-ellipse core-shaped resonator	65.3
[24]	super-ellipse core-shaped resonator	65.3
[25]	Hexagonal ring resonator	92.3
[26]	1-D PC structure	88.7
[22]	Z-shaped ring resonator	96
This work	ADF	104

## VI. CONCLUSION

In conclusion, a structure is proposed consisting of a ring resonator which is created on 2D photonic crystal. It is shown through simulations that the structure acts as an add-drop filter (ADF) and can be implemented in all-optical communication systems. The same structure can also act as refractive index and temperature sensor. Simulations are carried out using the PWE and FDTD method. The sensitivity is determined by shifts in the resonance wavelength as a function of the refractive index (RI) of air holes (for RI sensing) and silicon slab (for Temperature sensing). The designed sensor exhibits desirable features like (i) a narrow bandwidth of 1.5 nm, (ii) a high-quality factor of 1033, (iii) a low detection limit of  $3.6 \times 10^{-4}$  RIU at a resonance wavelength of 1550 nm (iv) high RI sensitivity of 407 nm/RIU and (v) high temperature sensitivity of 104 pm/K.

## ACKNOWLEDGMENT

Puja Sharma and Nilaksha Ghosh acknowledge University fellowship from the Central University of Jharkhand, Ranchi, INDIA.

## REFERENCES

- [1] S.G. Johnson, A. Mekis, S. Fan, and J.D. Joannopoulos, "Molding the flow of light," *Comput. Sci. Eng.*, Vol. 3, pp. 38–47, 2001.
- [2] I. Chremmos, O. Schwelb, and N. Uzunoglu, *Photonic Microresonator Research and Applications* Springer, 2010.
- [3] P. Sharma, M.M. Gupta, N. Ghosh, and S. Medhekar, "Optical add-drop filter based on square ring resonator consisting of octagon shape core." In: 2021 IEEE International Conference on Technology, Research, and Innovation for Betterment of Society (TRIBES) IEEE, pp. 1–5, 2021.
- [4] C. Guo, C. Wang, T. Ma, and F. Wang, "Ultra-compact and highly sensitive refractive index sensor based on a chalcogenide suspended slot hybrid plasmonic microring resonator," *Optik*, Vol. 274, pp. 170595 (1-9), 2023.
- [5] S. Chen, P. Pan, T. Xie, and H. Fu, "Sensitivity enhanced fiber optic temperature sensor based on optical carrier microwave photonic interferometry with harmonic Vernier effect," *Opt. Laser Technol.*, Vol. 160, pp. 109029 (1-6), 2023.
- [6] P. Sharma and S. Medhekar, "Ultra-compact photonic crystal nanocavity - based sensor for simultaneous detection of refractive index and temperature," *J. Opt.*, Vol. 52pp. 504–509, 2022.
- [7] M.A. Lifson and B.L. Miller, *Photonic crystals as robust label-free biosensors*, Springer, pp. 189–207, 2015.
- [8] N. Ghosh, P. Sharma, S. Medhekar, and M.M. Gupta, "Design and analysis of the pressure sensor based on 2D photonic crystal consisting of micro-cavity." In: 2021 IEEE International Conference on Technology, Research, and Innovation for Betterment of Society (TRIBES) IEEE, pp.1–4, 2021.
- [9] J.E. Baker, R. Sriram, and B.L. Miller, "Two-dimensional photonic crystals for sensitive microscale chemical and biochemical sensing," *Lab Chip*, Vol. 15, pp. 971–990, 2015.

- [10] J. Wang, S.X. Chew, S. Song, L. Li, L. Nguyen, and X. Yi, "On-chip simultaneous measurement of humidity and temperature using cascaded photonic crystal microring resonators with error correction," *Opt. Express*, Vol. 30, pp. 35608-35623, 2022.
- [11] P. Sharma and S. Medhekar, "Ring resonator - based highly sensitive chemical / biochemical sensor created on holes in silicon slab 2D photonic crystal," *J. Opt.*, pp. 1-6, 2023, 10.1007/s12596-023-01149-2.
- [12] Y. N. Zhang, Y. Zhao, and R. Q. Lv, "A review for optical sensors based on photonic crystal cavities," *Sensors Actuators, A Phys.*, Vol. 233, pp. 374-389, 2015.
- [13] F. Lotfi, N.S. Nourpour, R. Kheradmand, "High-sensitive plasmonic sensor based on Mach-Zehnder interferometer" *Opt. Laser Technol.*, Vol. 137, pp. 106809 (1-10), 2021.
- [14] P. Sharma, M. Mohan, N. Ghosh, and S. Medhekar, "Materials Today : Proceedings 2D photonic crystal based all-optical add-drop filter consisting of square ring resonator," *Mater. Today Proc.*, Vol. 66, pp. 3344-3348, 2022.
- [15] M. Bazian, "Photonic crystal add-drop filter: a review on principles and applications," *Photon. Netw. Commun.*, Vol. 41, pp. 57-77, 2021.
- [16] F. Hsiao and C. Lee, "A Nano-ring Resonator Based on 2-D Hexagonal-Lattice Photonic Crystals," *IEEE/LEOS International Conference on Optical MEMS and Nanophotonics*, Vol. 1, pp. 107-108, 2009.
- [17] T. Sreenivasulu, K. Bhowmick, S. Abdul Samad, T.I.R. Yadunath, T. Badrinarayana, G.M. Hegde, and T. Srinivas, "Photonic crystal ring resonator-based four-channel dense wavelength division multiplexing demultiplexer on silicon on insulator platform: design and analysis," *Opt. Eng.*, Vol. 57, pp. 046109 (1-9), 2018.
- [18] R. Antos, V. Vozda, and M. Veis, "Plane wave expansion method used to engineer photonic crystal sensors with high efficiency," *Opt. Express*, Vol. 22, pp. 2562-2577, 2014.
- [19] H. Alipour-banaei, M. Jahanara, and F. Mehdizadeh, "T-shaped channel drop filter based on photonic crystal ring resonator," *Int. J. Light Electron Opt.*, Vol. 125, pp. 5348-5351, 2014.
- [20] M. Radhouene, V.R.B. Monia, and S.R.V. Janyani, "Rounded square ring resonator based add drop filter for WDM applications using two dimensional photonic crystals," *Opt. Quantum Electron.*, Vol. 53, pp. 1-24, 2021.
- [21] C.T. Chou Chao and Y.F. Chou Chau, "Highly Sensitive Multichannel Fano Resonance-Based Plasmonic Sensor for Refractive Index and Temperature Sensing Application," *Photon.*, Vol. 10, pp. 82 (1-15) 2023.
- [22] A. Benmerkhi, A. Bounouioua, M. Bouchemat, and T. Bouchemat, "Analysis of a photonic crystal temperature sensor based on Z-shaped ring resonator," *Opt. Quantum Electron.*, Vol. 53, pp. 1-14, 2021.
- [23] Z. Liu, F. Sun, C. Wang, and H. Tian, "Side-coupled nanoscale photonic crystal structure with high-Q and high-stability for simultaneous refractive index and temperature sensing," *J. Mod. Opt.*, Vol. 66, pp. 1339-1346, 2019.
- [24] M. Radhouene, M.K. Chhipa, M. Najjar, S. Robinson, and B. Suthar, "Novel design of ring resonator based temperature sensor using photonics technology," *Photon. Sensors*, Vol. 7, pp. 311-316, 2017.
- [25] R. Zegadi, L. Ziet, and A. Zegadi, "Design of High Sensitive Temperature Sensor Based on Two-Dimensional Photonic Crystal," *Silicon*, Vol. 12, pp. 2133-2139, 2020.
- [26] Y.H. Chen, W.H. Shi, L. Feng, X.Y. Xu, and M.Y. Shang-Guan, "Study on simultaneous sensing of gas concentration and temperature in one-dimensional photonic crystal," *Superlattices Microstruct.*, Vol. 131, pp. 53-58, 2019.



**Puja Sharma** has received B.Sc. (Physics) from Marwari College, Ranchi in 2016 and M.Sc. in Physics with Specialization in Electronics in 2018 from Department of Physics, Ranchi University Ranchi, Jharkhand. Currently, she is a doctoral candidate at the Department of Physics, Central University of Jharkhand, Ranchi, India.

Her area of research interest includes photonic devices, sensors and all optical switching devices.



**Nilaksha Ghosh** has received Bachelor Degree from Calcutta University, Kolkata in 2014 and Master degree in Physics with Specialization in Condensed Matter Physics (CMP) in 2017 from Madurai Kamraj University, Madurai Tamilnadu. He is currently pursuing Ph.D. in Department of Physics, Central University of Jharkhand, Ranchi, India.

His area of research interest includes photonic sensors and all optical switching and logic devices.



**Man Mohan Gupta** completed his M.Sc. from Dayalbagh Educational Institute, Agra in 2007

and Ph.D. from Central University of Jharkhand, India, in 2017. Currently he is serving as an assistant professor at the Department of Physics, Tata College, Chaibasa, West Singh Bhum, India. His area of research includes photonic crystal and optical waveguide based devices.



**Sarang Medhekar** received his M.Sc. and Ph.D. degrees in physics from Devi Ahilya University, Indore, Madhya Pradesh, India, in 1991 and 1996, respectively. At the present he is working as professor in the Department of Physics, Central University of Jharkhand, Ranchi, India.

His current areas of research interest are photonic devices, all-optical switching, optical computing, photonic nanostructures (photonic crystals) and optical soliton propagation.